

PAPER • OPEN ACCESS

Phase formation and electrical properties of reactively sputtered Fe_{1-x}O thin films

To cite this article: S Evertz *et al* 2024 *J. Phys. D: Appl. Phys.* **57** 065302

View the [article online](#) for updates and enhancements.

You may also like

- [SolidState Coulometric Titration: Critical Analysis and Application to Wüstite](#)
Robert A. Giddings and Ronald S. Gordon
- [THE ROLE OF CARBON IN EXTRASOLAR PLANETARY GEODYNAMICS AND HABITABILITY](#)
Cayman T. Unterborn, Jason E. Kabbes, Jeffrey S. Pigott et al.
- [Rate Controlling Step in the Reduction of Iron Oxides: Kinetics and Mechanism of Wüstite-Iron Step in \$\text{H}_2\$, CO and \$\text{H}_2/\text{CO}\$ Gas Mixtures](#)
Abdel-Hady A. El-Geassy

Phase formation and electrical properties of reactively sputtered Fe_{1-x}O thin films

S Evertz¹, N Nicolin¹, N Cheng¹, D Primetzhofer² , J P Best^{1,*}  and G Dehm^{1,*}

¹ Max-Planck-Institut für Eisenforschung GmbH, Max-Planck-Str. 1, 40237 Düsseldorf, Germany

² Department of Physics and Astronomy, Uppsala University, 752 36 Uppsala, Sweden

E-mail: j.best@mpie.de and dehm@mpie.de

Received 25 May 2023, revised 23 October 2023

Accepted for publication 7 November 2023

Published 16 November 2023



Abstract

Wüstite, Fe_{1-x}O , is a crucial phase for the transition to CO_2 -free steel manufacturing as well as promising for electrochemical applications such as water splitting and ammonia synthesis. To study the effect of interfaces in these applications, thin-film model systems with defined interfaces are ideal. Previous studies lack a description of the growth mechanism to obtain Fe_{1-x}O thin films. Here, we investigate the phase formation of metastable Fe_{1-x}O during reactive magnetron sputtering while systematically varying the O_2/Ar flow ratio from 1.8% to 7.2% and the pressure–distance product between 3.5 and 7.2 Pa cm. If bulk diffusion is minimized, thin films containing 96 vol.% wüstite and 4 vol.% Fe as impurity phase were achieved. Therefore, the wüstite phase formation appears to be surface diffusion dominated. To reveal the influence of impurity phases in wüstite on the electrical resistivity, systematic electrical resistivity measurements while cooling *in situ* were performed for the first time. The electrical resistivity was lower than that of single crystals of the respective iron oxides. This is attributed to the formation of Fe-rich layers at the substrate–film interface, which serve as additional conduction paths.

Supplementary material for this article is available [online](#)

Keywords: wüstite, physical vapor deposition, reactive sputtering, electrical properties

1. Introduction

Fe_{1-x}O , or wüstite, is a critical material for the CO_2 -free, hydrogen-based reduction of iron ore, as it is the last oxide in the reaction chain before metallic iron is obtained [1]. At the same time, this last reduction step from Fe_{1-x}O to iron is rate limiting, due to dissociation of wüstite at the wüstite–iron

interface and diffusion of the reacting species to the reaction front [2]. On the other hand, Fe_{1-x}O is an interesting material to catalyze hydrogen evolution reactions. Charvin *et al* report a water-hydrolysis reaction between wüstite and steam, forming Fe_3O_4 and H_2 , and the subsequent thermal reduction back to wüstite powered by solar light [3]. For ammonia synthesis, wüstite-based catalysts outperform conventional magnetite-based catalysts [4]. For these catalytic applications, charge transfer and thus electrical properties as well as phase purity is important. This work, therefore, aims to establish a relationship between phase purity and electrical conductivity of Fe_{1-x}O thin films.

Fe_{1-x}O exists in the fcc rocksalt-structure and is metastable under ambient conditions [5]. Its non-stoichiometry due to Fe

* Authors to whom any correspondence should be addressed.



Original content from this work may be used under the terms of the [Creative Commons Attribution 4.0 licence](#). Any further distribution of this work must maintain attribution to the author(s) and the title of the work, journal citation and DOI.

deficiency causes defects to be inherent to the atomic structure [5]. The high defect concentration of Fe vacancies as well as Fe^{3+} interstitials allows the interaction of defects and formation of clusters [6], which makes wüstite interesting in terms of diffusion as well as electrical properties. The semiconducting Fe_{1-x}O exhibits non-linearity in the electrical resistivity as a function of x , which may originate in modifications of the defect structure [7]. For charge transport, intrinsic charge carriers hop via Fe^{2+} and Fe^{3+} sites [6, 8], which is dependent on temperature as the hopping mechanism is thermally activated [9]. In addition, vacancies create trapping sites [10], where charge carriers reside longer [11], thereby increasing the electrical resistivity [10].

Fe_{1-x}O thin films have been synthesized before from magnetite targets [12] as well as by reactive magnetron sputtering [13–16]. Mauvernay *et al* report that by controlling the ion energy, reducing growth conditions can be created to synthesize Fe_{1-x}O from a Fe_3O_4 target [12]. Other authors employ reactive magnetron sputtering by sputtering Fe_{1-x}O from a metallic Fe target in an Ar– O_2 atmosphere, whereby either the O_2 flow [13–16], film thickness [14, 15] or substrate temperature [15] is varied. While some papers miss clear information about the actual O_2/Ar flow ratio [13, 16] or target power density [13, 16], other studies indicate a narrow parameter range for the synthesis of Fe_{1-x}O films, because impurity phases such as Fe and Fe_3O_4 form readily [14, 15]. These studies lack a description of both the growth mechanism to obtain Fe_{1-x}O thin films and convergence on a recipe for the synthesis of Fe_{1-x}O thin films. Therefore, the aim of this work is to reveal the dominating mechanism for the growth of Fe_{1-x}O during magnetron sputtering by systematic variations of the O_2/Ar ratio in the sputtering gas; the pressure–distance product as well as temperature and film thickness. In the second part of this work, the effect of impurity phases on the electrical properties is analyzed.

2. Experimental methods

Fe_{1-x}O thin films were synthesized on (001) Si wafers with a resistivity of $200\ \Omega\text{m}$ —which is significantly higher than the expected resistivity of the thin films and minimizes the influence of the substrate in electrical resistivity measurements—by reactive magnetron sputtering in the HV chamber of the Bestec GmbH (Berlin, Germany) multi-technique deposition cluster at the Max-Planck-Institut für Eisenforschung GmbH, Düsseldorf, Germany [17], with a base pressure lower than $4.4 \cdot 10^{-5}$ Pa. A 3'' Fe target with 99.95% purity (MaTecK GmbH, Jülich, Germany) and a thickness of 1 mm was powered by direct current power supply (Maris GS10/800, ADL GmbH, Darmstadt, Germany) with a power density of $5.5\ \text{W cm}^{-2}$. Thereby, the magnetic field strength in front of the magnetron was 311 mT. While keeping the working gas pressure constant at $3 \cdot 10^{-1}$ Pa and the Ar gas flow at 55 sccm, the O_2 gas flow was varied systematically as indicated in table 1. This process gas flow translates to a variation of the O_2/Ar flow ratio $f_{\text{O}_2}/f_{\text{Ar}}$ between 1.8% and 7.2% under the assumption of an ideal gas.

Table 1. Deposition parameters for the synthesis of Fe_{1-x}O thin films.

Parameter	Values
Target power density	$5.5\ \text{W cm}^{-2}$
Base pressure	$<4.4 \cdot 10^{-5}$ Pa
Working gas pressure	$3 \cdot 10^{-1}$ Pa
Ar flow	55 sccm
O_2 flow	1–4 sccm
Target-to-substrate distance	112–239 mm
Substrate heating	Non-active & $320\ ^\circ\text{C}$
Substrate rotation	20 rpm

Additionally, the target-to-substrate distance, substrate temperature and deposition time were varied systematically. The deposition parameters are summarized in table 1.

The phase formation was analyzed in a GE Seifert diffractometer in grazing incidence geometry with an incidence angle of 2° . A parallel beam with Co $K\alpha$ radiation and a GE Meteor 0D energy dispersive point detector was used. The microstructure was investigated on cross-sections in a Zeiss Gemini (Oberkochen, Germany) scanning electron microscope (SEM) as well as by STEM images and energy-dispersive x-ray spectroscopy (EDS) maps acquired in a probe-corrected FEI Titan Themis 60-300 transmission electron microscope (TEM, Thermo Fisher Scientific) at 300 kV, equipped with a high-brightness field emission gun, a gun monochromator, and a Super X detector. TEM samples were lifted out by focused ion beam (FIB) techniques in a Scios 2 HiVac DualBeam SEM/FIB (Thermo Fisher Scientific) and thinned starting with a Ga ion beam voltage and current of 30 kV and 0.1 nA and finishing with 5 kV and 16 pA. The EDS data was analyzed using the hyperspy python library [18]. To determine the composition, the intensities of the Fe $K\alpha$ and O $K\alpha$ lines were considered. The k factor was calculated using the average chemical composition of the sample as determined by time-of-flight elastic recoil detection analysis (ToF-ERDA).

Based on the concentrations obtained from ToF-ERDA for Fe and O, $c_{\text{Fe,ERDA}}$ and $c_{\text{O,ERDA}}$, as well as the integrated intensities of the Fe $K\alpha$ and O $K\alpha$ peak, i_{Fe} and i_{O} , the k factor can be calculated by equation (1). The composition in the EDS measurements can subsequently be calculated based on the same equation, then with unknown compositions and known k

$$k = \frac{c_{\text{O}} i_{\text{Fe,ERDA}}}{c_{\text{Fe}} i_{\text{O,ERDA}}}. \quad (1)$$

ToF-ERDA for chemical composition depth profiling was performed at the Tandem Laboratory of Uppsala University, Sweden [19]. 36 MeV $^{127}\text{I}^{8+}$ primary ions at an incidence angle of 22.5° with respect to the film surface were used. Recoils were detected in forward direction, again at an angle of 22.5° with respect to the film surface. The angle between the primary ion beam and the detector telescope was 45° . Time–energy coincidence spectra were recorded with a solid-state detector and further details on the detection system can be found in [20]. Conversion of the coincidence spectra to depth

profiles was done with CONTES [21]. Stoichiometric TiN and Al_2O_3 reference samples were also measured to correct for potential systematic uncertainties and the maximum statistical uncertainty was $<0.3\%$ relative to the deduced values.

The electrical resistivity was measured with the van der Pauw method [22] in a Linkam HFS600 temperature control stage equipped with four tungsten probes supported by springs. Ag contacts were deposited by electron beam evaporation at the corners of the 1×1 cm samples. Employing a liquid nitrogen pump and as well as heating controller, the temperature was varied between -110°C and 250°C with a heating rate of 5 K min^{-1} . For measurements, the temperature was kept constant for 3 min, whereof the first minute was used for temperature equilibration. Current–voltage curves were measured by sweeping currents between -1 and $+1$ mA with a Keithley 6221 and measuring the voltage with a nanovoltmeter Keithley 2182 A (Tektronix, Beaverton, USA). Two specimens were measured per sample to ensure reproducibility.

3. Results and discussion

3.1. Phase formation

To investigate the phase formation of Fe_{1-x}O during reactive magnetron sputtering, this study focusses on the O_2/Ar flow ratio and the pressure–distance product by the target-to-substrate distance. X-ray diffraction pattern for samples synthesized at O_2/Ar flow ratios $f_{\text{O}_2}/f_{\text{Ar}}$ varying between 4.7% and 7.3% are shown in figure 1(a). Between 4.7% and 5.1% O_2 in the sputtering gas, reflections of $\alpha\text{-Fe}$ are clearly visible next to those of Fe_{1-x}O at 52° . Increasing $f_{\text{O}_2}/f_{\text{Ar}}$ to 5.1 and 5.3%, the Fe_{1-x}O reflections become dominant, although a shoulder at 52° remains, which can be attributed to remaining $\alpha\text{-Fe}$. For $f_{\text{O}_2}/f_{\text{Ar}}$ between 5.8% and 7.3%, Fe_3O_4 starts to form as impurity phase next to Fe_{1-x}O and is the dominant phase at 7.3% $f_{\text{O}_2}/f_{\text{Ar}}$.

Considering the volume fraction of each phase, estimated by the ratio of the sum of the area below the reflections of the individual phase relative to the total area of all reflections, a maximum of the Fe_{1-x}O volume fraction can be identified (figure 1(b)). The Fe content is decreasing from 46 vol.% to 4 vol.% between 4.7% and 5.5% $f_{\text{O}_2}/f_{\text{Ar}}$. Starting from 5.8% $f_{\text{O}_2}/f_{\text{Ar}}$, magnetite adds to the amount of impurity phases, which increases from 4 vol.% up to 100 vol.% at 7.3% $f_{\text{O}_2}/f_{\text{Ar}}$. Thus, a maximum Fe_{1-x}O content of 96 vol.% is reached between 5.5% and 5.6% $f_{\text{O}_2}/f_{\text{Ar}}$.

Considering the pressure–distance product $p\cdot d$ at a fixed $f_{\text{O}_2}/f_{\text{Ar}}$ of 4.5% in the working gas, x-ray diffraction patterns (figure 2(a)) show a shift to higher oxide states with increasing $p\cdot d$. While at 3.5 Pa cm the sample contains 97 vol.% wüstite (figure 2(b)), magnetite already forms at 4.4 Pa cm. At 7.2 Pa cm, a pure magnetite film is formed.

In addition to O_2/Ar flow ratio and pressure–distance product, the substrate temperature and the film thickness can affect the phase formation. A sample deposited at a substrate temperature of 320°C and with a $f_{\text{O}_2}/f_{\text{Ar}}$ of 4.5% at a $p\cdot d$ of 3.5 Pa cm contains magnetite and $\alpha\text{-iron}$ (see supplementary

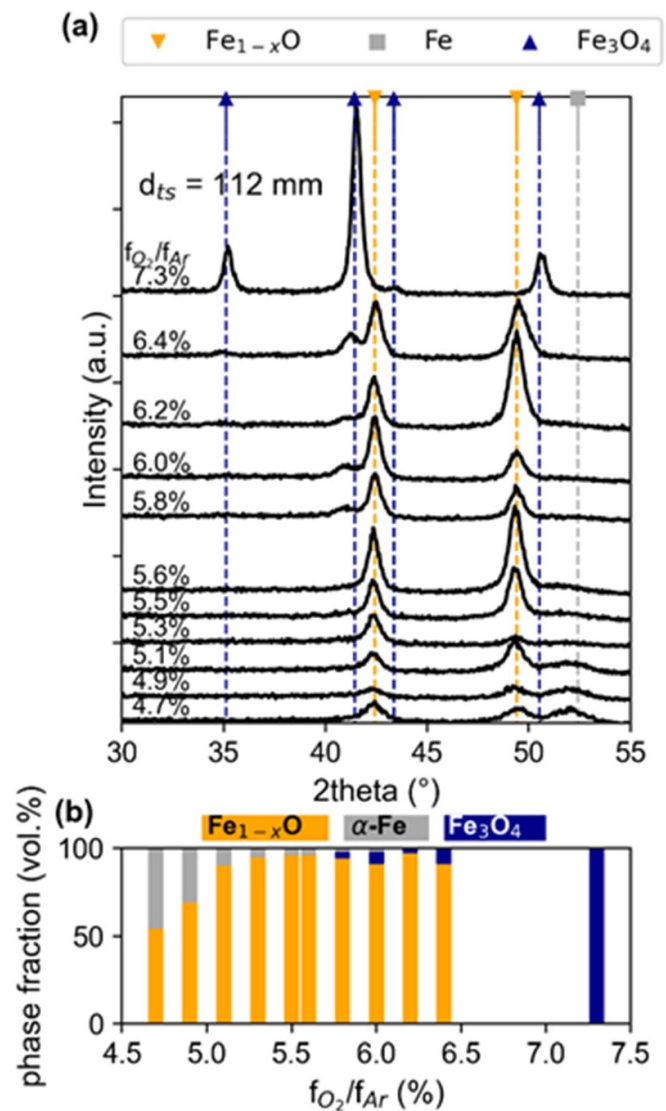


Figure 1. (a) X-ray diffraction patterns of samples deposited at different O_2 flow at a pressure–distance product of 3.5 Pa cm and (b) phase fraction based on relative peak areas.

material, figure S1), which is the stable phase mixture in thermodynamic equilibrium at 320°C [23]. Formation of the thermodynamically stable phase mixture during deposition may be caused by the activation of bulk diffusion due to the increased surface temperature of 320°C .

Systematically changing the deposition time to obtain variations of film thickness between 300 and 1400 nm only marginally changes the phase fraction of wüstite by around 6 vol.% (suppl. material figure S2). This result is in contrast to the report by Chin and Chiang [14], where the influence of gas mixture and film thickness on the phase formation of iron oxides was investigated. In their experimental setup, for an $f_{\text{O}_2}/f_{\text{Ar}}$ ratio of 2% Fe_{1-x}O thin films were observed between 120 and 200 nm film thickness [14]. Therewith, films in the present study are all thicker than the ones investigated in [14]. Thus, the influence of interface and surface energy on the phase formation for films thicker than 300 nm seems to be small.

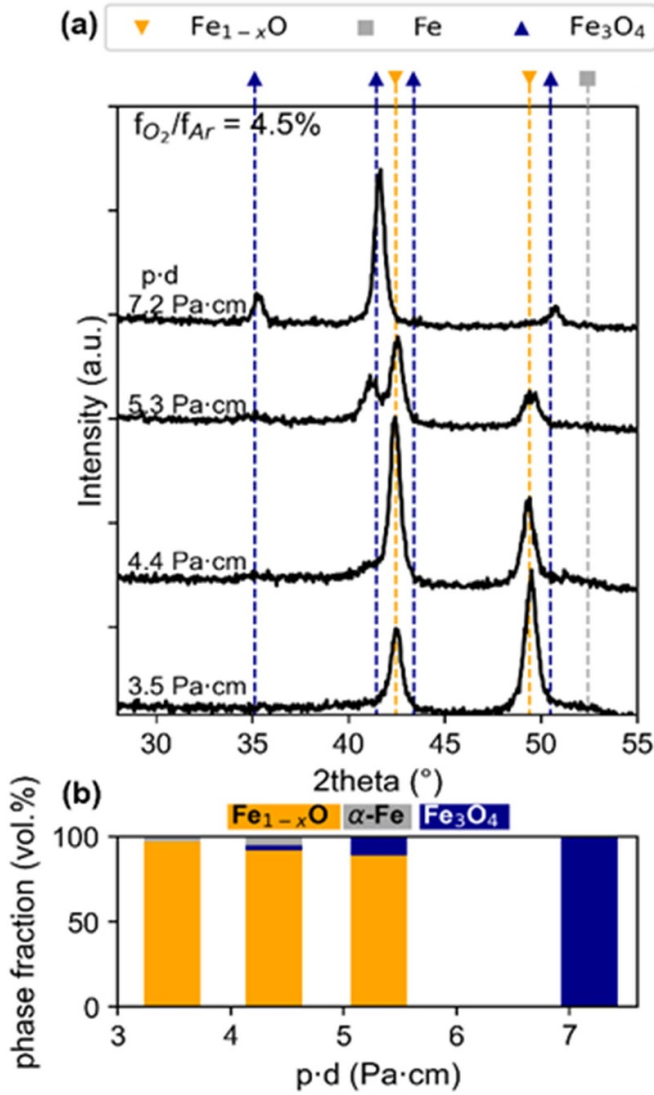


Figure 2. (a) X-ray diffraction patterns of samples deposited at different pressure–distance products ($p \cdot d$) at a f_{O_2}/f_{Ar} of 4.5% and (b) phase fraction based on relative peak areas.

Based on this parameter study, the growth of $Fe_{1-x}O$ appears to be surface controlled. The influence of the oxygen flow can be intuitively understood by the supply of a sufficient amount of oxygen. Chambers [24] reported a trade-off between oxygen dissociation at the growing film surface and the growth rate. If the dissociation of O_2 is faster than the incorporation rate, an excess of oxygen is available and higher oxidation states of Fe are formed. If the dissociation rate is slower than the incorporation rate, $Fe_{1-x}O$ can form [24]. This trade-off is of particular importance if the sputtering mode is metallic instead of poisoned, i.e. the target is not oxidized and therefore metallic species instead of oxide species are sputtered. These metallic species then need to be oxidized in the plasma or after condensation at the substrate surface to obtain oxide films, where Chambers [24] model is valid. The state of the target can be understood by analysis of the target poisoning curve (figure 3).

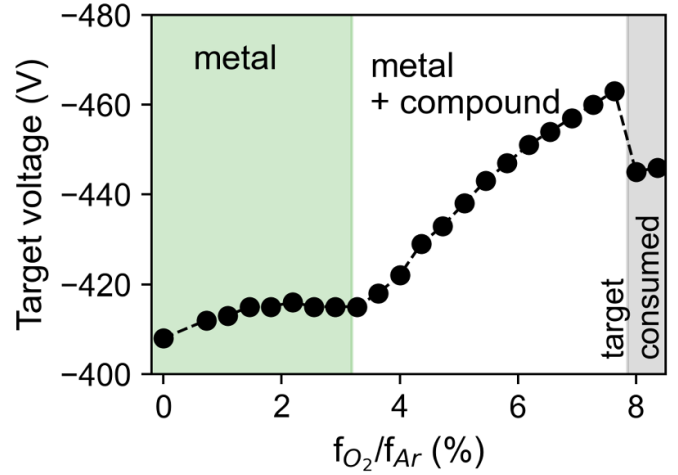


Figure 3. Target poisoning curve for an Fe target sputtered with 250 W (DC). The total gas pressure was kept constant at $3 \cdot 10^{-1}$ Pa, while the flow of O_2 was increased stepwise to change the O_2/Ar ratio.

Figure 3 shows the target voltage as a function of f_{O_2}/f_{Ar} during DC sputtering. A decrease in voltage indicates the formation of oxides at the target surface, starting at an f_{O_2}/f_{Ar} of 3.3%. The sudden voltage drop at $f_{O_2}/f_{Ar} = 8\%$ is caused by sputtering through the race-track of the target, indicating that the target is consumed. Thus, the experiment is stopped at this point. Due to consumption of the target the final, completely oxidized, target surface cannot be reached. However, this poisoning curve shows that all samples in this work ($f_{O_2}/f_{Ar} = 4.5\% - 7.3\%$) are sputtered in a mixed metallic and compound mode, where the sputtered species are not entirely oxidized at the target surface. Hence, one can infer that the oxidation of Fe occurs at least partially at the surface of the growing film.

A measure for the probability of collisions of sputtered particles with the ambient gas particles, is the pressure–distance product $p \cdot d$. Frequent collisions between particles lead to thermalized motion instead of the initial ballistic transport mode, i.e. a decrease of energy of the sputtered particles with increasing $p \cdot d$ [25]. As $Fe_{1-x}O$ forms only at low $p \cdot d$, the energy of the particles arriving at the substrate is larger than in the case of thermalized motion and allows surface diffusion of the adsorbed species. Hence, surface diffusion seems to be crucial for the synthesis of $Fe_{1-x}O$. Bulk diffusion, which can be activated by an increased substrate temperature, leads to the formation of magnetite, which is thermodynamically stable. From these considerations, one can conclude that the growth of $Fe_{1-x}O$ thin films is surface diffusion controlled.

3.2. Composition and microstructure

The composition on selected samples was measured by time-of-flight elastic recoil detection analysis (ToF-ERDA). For the remaining samples, standard-based EDS was used with ToF-ERDA data as a reference. The composition (table 2) is Fe-rich for the samples with large volume fraction of metallic

Table 2. Composition and thickness of iron oxide thin films.

f_{O_2}/f_{Ar} (%)	Fe (at.%)	O (at.%)	Thickness (nm)
4.7	65 ^b	35 ^b	649 ± 57
4.9	58 ^a	42 ^a	599 ± 13
5.1	59 ^b	41 ^b	626 ± 14
5.3	54 ^a	46 ^a	688 ± 24
5.5	55 ^a	45 ^a	664 ± 12
5.6	54 ^a	46 ^a	664 ± 16
5.8	52 ^a	48 ^a	721 ± 8
6.0	53 ^a	47 ^a	688 ± 20
6.2	51 ^a	49 ^a	666 ± 16
6.4	48 ^b	52 ^b	707 ± 26
7.3	40 ^b	60 ^b	727 ± 41

$p \cdot d$ (Pa cm)	Fe (at.%)	O (at.%)	Thickness (nm)
3.5	55 ^a	45 ^a	699 ± 42
4.4	51 ^b	49 ^b	368 ± 1
5.3	51 ^b	49 ^b	942 ± 1
7.2	50 ^b	50 ^b	238 ± 16

^a ERDA.^b standard-based EDS.

iron as impurity phase. Between 5.5% and 5.8% f_{O_2}/f_{Ar} , the composition does not change significantly with increasing f_{O_2}/f_{Ar} , but scatters around 54 at.% Fe. Thus, all samples containing $Fe_{1-x}O$ are over-stoichiometric with respect to Fe, while an Fe deficiency would be expected for wüstite [5]. However, as α -Fe has been identified as an impurity phase in all $Fe_{1-x}O$ containing samples, the excess Fe in the composition can be rationalized to originate from this impurity phase, as the composition is averaged over the film and not phase-sensitive. Due to the absence of a depth gradient of chemical composition, as detected by ToF-ERDA, α -Fe seems to be homogeneously distributed throughout the thickness of the film. For f_{O_2}/f_{Ar} of 6.2% and higher, the Fe-content is decreasing, which is consistent with the formation of Fe_3O_4 , which is oxygen-rich compared to $Fe_{1-x}O$ and α -Fe.

For further investigations, samples synthesized at O_2/Ar flow ratios of 5.1%, 5.3%, 5.5%, and 5.8% were selected for detailed microstructural analysis (figure 4), as these samples contain the largest volume fractions of $Fe_{1-x}O$. The high-angle annular dark-field (HAADF) image of 5.1% f_{O_2}/f_{Ar} sample (figure 4(a)) shows a columnar microstructure with a column width of 105 ± 18 nm. The film is dense with negligible porosity. This microstructure is consistent with the zone I of Thornton's structure zone model [26]. However, based on the deposition pressure and homologous temperature $T_h = 0.17$, the position in the structure zone model is very close to the border between zone I and zone T [26]. Growth in zone T is dominated by ion bombardment induced adatom mobility [27, 28], which is consistent with the low $p \cdot d$ growth conditions required for a maximum wüstite content as discussed in section 3.1. However, small changes in synthesis parameters such as the sputtering gas mixture may lead to changes in the microstructure.

For the samples synthesized at f_{O_2}/f_{Ar} of 5.3 and 5.5% in figures 4(b) and (c), the columns in the microstructure are less clearly defined and contain a fiber-like substructure, making quantification of the grain size challenging. However, the fiber-like substructure of the grains indicates a transition from zone I to zone T in the structure zone model [26, 28], triggered by the enhanced oxygen content and thereby changes average specific mass of the sputtering gas. In contrast to the sample deposited at $f_{O_2}/f_{Ar} = 5.1\%$, pores are clearly visible for $f_{O_2}/f_{Ar} = 5.3\%$ (figure 4(b)) by their dark contrast in the HAADF image and corresponding bright contrast in the bright field image (suppl. material figure S3), where they appear needle-shaped between the grains with a distance of 52 ± 27 nm between the pores. This pore separation distance infers a grain size of about half the size observed at 5.1% f_{O_2}/f_{Ar} . For $f_{O_2}/f_{Ar} = 5.5\%$, only isolated pores are present. Also, for $f_{O_2}/f_{Ar} = 5.8\%$ (figure 3(d)) the microstructure is feather-like but dense. Therefore, columns are not clearly distinguishable to determine the column size.

EDS maps of Fe and O in figure 4 reveal that the films are chemically inhomogeneous. In the sample deposited at $f_{O_2}/f_{Ar} = 5.1\%$, shades in the EDS maps (figure 4(a)) correspond with the grains visible in the HAADF image and indicate the existence of Fe-rich and Fe-depleted grains. Moreover, at the bottom of the film an Fe-rich layer is found (EDS profiles in figure S4). For $f_{O_2}/f_{Ar} = 5.3\%$ during deposition (figure 4(b)), the elemental distribution seems more homogeneous. However, also for this sample, enrichment of Fe is observed at the interface to the substrate as well as the surface of the film. At $f_{O_2}/f_{Ar} = 5.5\%$ (figure 4(c)), the Fe-rich layer is not visible in the EDS maps, while iron enrichment close to the substrate is less pronounced compared to the other samples (figure S4). Signal above the position of the surface, which is the same in both HAADF and EDS maps, are artifacts of the measurement. Zooming in on the surface layer confirms that the film is terminated by a layer consisting of Pt and Fe (figure S5). This could indicate the formation of an intermetallic phase by the reaction of Fe from the film with the Pt applied as protecting layer during sample preparation in FIB. At the highest $f_{O_2}/f_{Ar} = 5.8\%$, the Fe-rich interface layer appears again. In addition, an Fe gradient towards the surface seems to exist.

The x-ray diffraction results (figure 1) indicated that Fe as an impurity phase is present in all $Fe_{1-x}O$ samples. The majority of this impurity phase seems to be located in the layers at the substrate-film interface (figure 4). The formation of Fe at the substrate interface suggests that the arriving species are not entirely oxidized. Based on the target poisoning curve (figure 3), this is consistent with the partially poisoned target for the f_{O_2}/f_{Ar} ratios of 5.1%–5.8%, which are relevant for figure 4. The sputtered, metallic species seem to arrive at the surface of the substrate or growing film and oxidize after incorporation into the growing film. The formation of the Fe-rich layer indicates a delayed oxidation, which can be understood based on the notion of Chambers [24], that slow dissociation of O_2 at the anode surface leads to the formation of Fe or $Fe_{1-x}O$. The O_2 dissociation at the pristine Si/SiO₂ surface, however, seems to be too slow for the formation of $Fe_{1-x}O$, thus forming

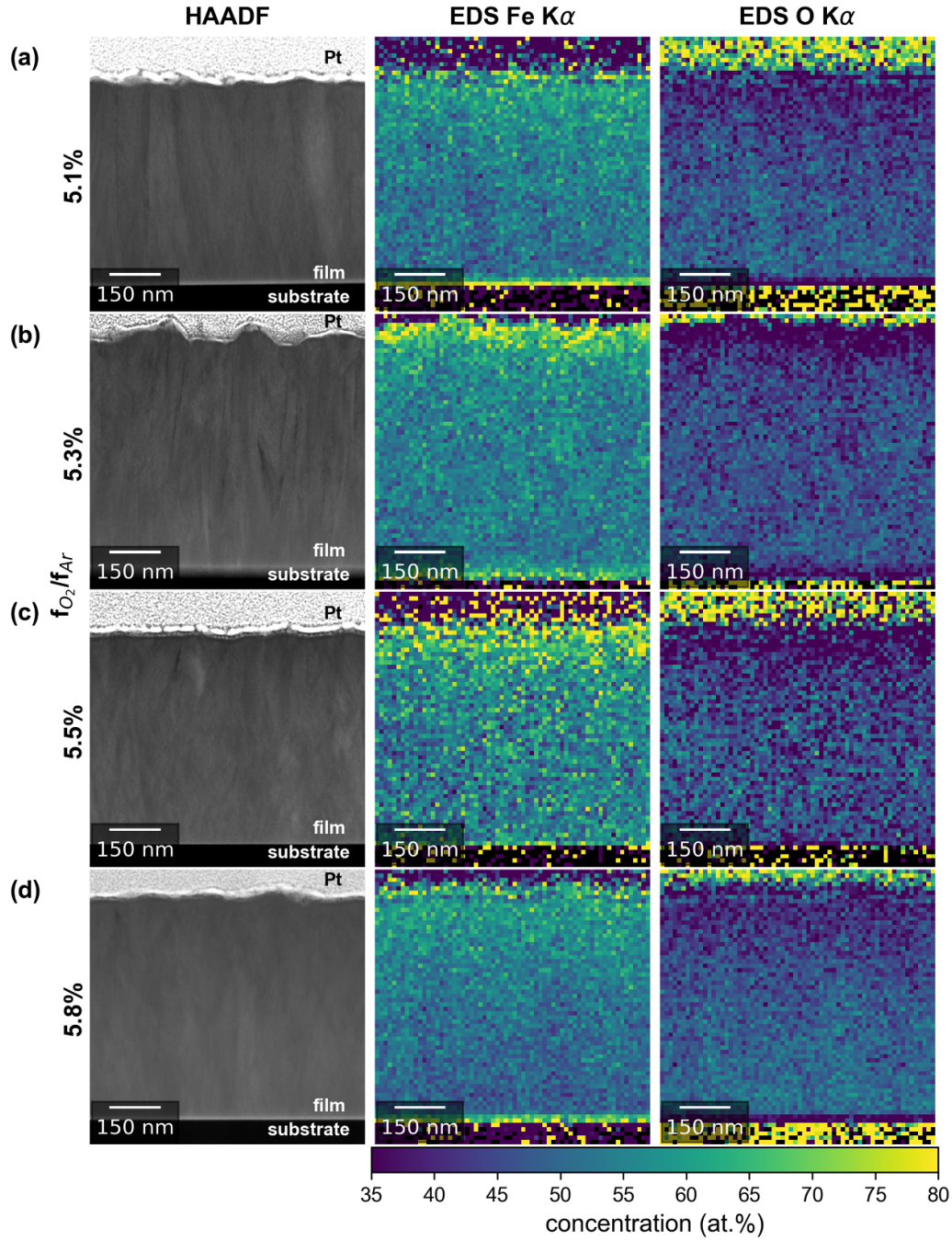


Figure 4. Microstructure of selected samples, showing HAADF, and EDS maps of Fe and O for samples synthesized with f_{O_2}/f_{Ar} of 5.1% (a), 5.3% (b), 5.5% (c) and 5.8% (d). Disperse yellow pixels observed at the interfaces in the EDS maps are expected to be a measurement artifact.

the Fe-rich layer. With an initial, Fe-rich layer, dissociation of O_2 seems to be enhanced and a more complete oxidation to $Fe_{1-x}O$ possible. Therefore, to avoid the formation of the Fe layer, a thorough understanding of the initial stages of film growth is necessary and is the topic of future work in this area.

3.3. Electrical resistivity

The electrical properties of the selected samples are presented in figure 5 and represent the average of two measurements

series on individual samples per thin film. While the slopes in both measurements for each sample are consistent, scattering between individual values at given temperature as large as 65% does occur, which may be attributed to the quality of the contacts as well as to the storage time between the individual measurements, causing further surface oxidation. The electrical resistivity (figure 5(a)) decreases with increasing temperature for the sample synthesized at a f_{O_2}/f_{Ar} of 5.5%. This is consistent with the expected temperature behavior for a semiconductor such as wüstite [29]. The resistivity of

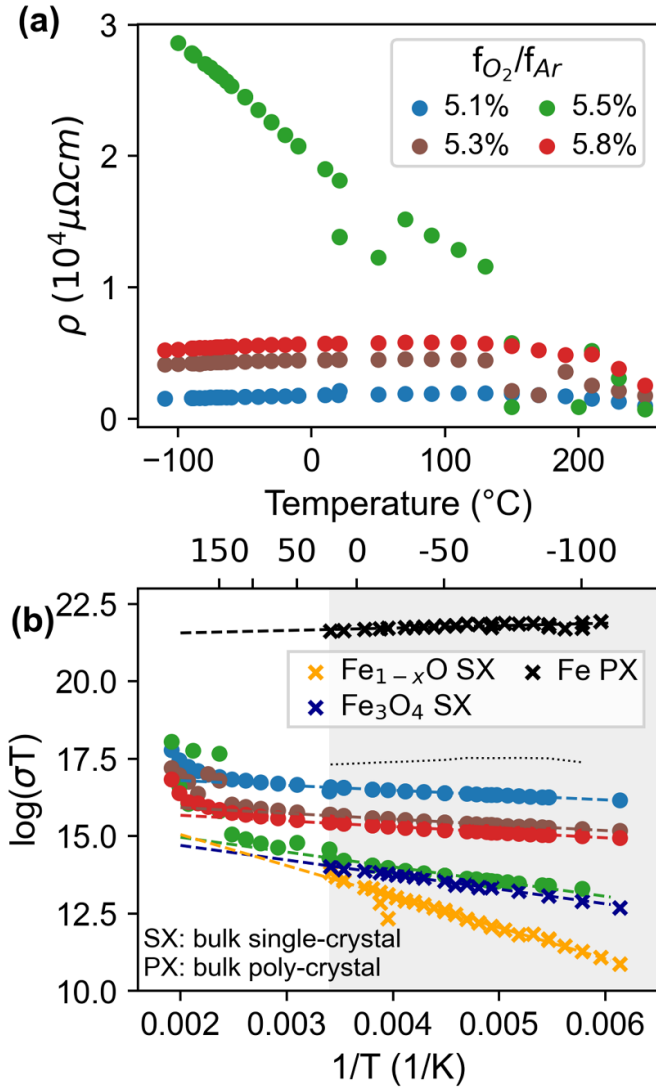


Figure 5. Electrical properties of Fe_{1-x}O thin films. (a) Resistivity as a function of temperature. (b) Arrhenius plot of electrical conductivity times temperature. The gray shaded area marks the temperature range considered for fitting, dashed lines indicate the fit to the data based on a model by Gartstein and Mason [29]. For reference, 'x' mark data for oxide single crystals and polycrystalline bulk iron. The black dotted line in (b) indicates a mechanical mixing model.

the other three samples, with synthesis conditions $f_{\text{O}_2}/f_{\text{Ar}}$ of 5.1, 5.3, and 5.8%, does not change strongly between -110°C and 100°C and decreases irreversibly at temperatures above 150°C . This irreversible change is caused by the decomposition of Fe_{1-x}O into Fe and Fe_3O_4 , which are the thermodynamically stable phases at temperatures below 560°C (see suppl. material figure S6). However, the temperature behavior below 100°C resembles more strongly a metallic response than a semiconductor.

Based on small polaron hopping via defect clusters, Gartstein and Mason proposed a mechanism of charge transport that depends on an activation energy [29]. Based on their model, and assuming that wüstite is the decisive phase for charge transport in the present samples, the activation energy

Table 3. Activation energy E_a for charge hopping based on the electrical conductivity model for wüstite by Gartstein and Mason [29].

$f_{\text{O}_2}/f_{\text{Ar}}$ (%)	E_a (meV)
5.1	13.4 ± 0.2
5.3	16.0 ± 0.4
5.5	33.8 ± 1.4
5.8	15.7 ± 0.4
Fe_3O_4	40.6 ± 0.7
Fe_{1-x}O	86.3 ± 3.0
Fe	$(-6.8 \pm 0.7)^a$

^a Note that the model is invalid for metals.

for charge transport was determined from the Arrhenius plot of electrical conductivity times temperature (figure 5(b)). The activation energies are listed in table 3. The activation energy for the sample synthesized at $f_{\text{O}_2}/f_{\text{Ar}}$ of 5.5%, i.e. the sample with 96 vol.% wüstite, is approximately twice as high as for the other samples.

For comparison with bulk values, in figure 5(b) the electrical conductivity of bulk poly-crystalline Fe and single-crystal Fe_3O_4 and Fe_{1-x}O are plotted in addition to the thin film values. As can be expected from the Fe impurity phase, the electrical conductivity of the thin films is between the conductivities of Fe and Fe_{1-x}O . Coincidentally, the conductivity of the sample containing 96 vol.% wüstite and 4 vol.% Fe is close to the values for single-crystalline Fe_3O_4 . The increasing conductivity of the Fe_3O_4 single crystal with temperature is consistent with literature, while at higher temperatures than investigated here the conductivity becomes nearly temperature independent due to the temperature dependence of its activation energy [6]. Activation energies (table 3) of the oxides differ by a factor of 2, with Fe_{1-x}O requiring the higher activation energy for charge hopping. For Fe, the apparent activation energy is negative, however, the Arrhenius-type model is not applicable for metals. Thus, the value for Fe can be neglected, although it represents the opposite temperature behavior of electrical conduction compared to semiconductors, which is consistent with theory.

The electrical conductivity deviates from the weighted average of the resistivity of the individual phases, as would be the case for a random mechanical mixture [30]. However, the electrical conductivity of the iron oxide thin films can be understood by the iron layer at the interface as well as the grain boundaries in the polycrystalline films. The Fe layer and the Fe_{1-x}O thin film are comparable to two resistances connected in parallel. Weighting the resistivities by the fraction of the iron layer on the overall film thickness, equation (2) is obtained for the resistivity of the entire film:

$$\rho = \left(\frac{x}{\rho_{\text{Fe}}} + \frac{1-x}{\rho_{\text{Fe}_{1-x}\text{O}}} \right)^{-1} \quad (2)$$

$$x = \frac{d_{\text{Fe}}}{d}. \quad (3)$$

Here, ρ , ρ_{Fe} , $\rho_{\text{Fe}_{1-x}\text{O}}$ and d , d_{Fe} and $d_{\text{Fe}_{1-x}\text{O}}$ are resistivity and thickness of the entire film, iron and wüstite, respectively. Using the values of the single crystals from figure 5(b), thereby neglecting the influence of defects present in the sputtered samples, resistivities close to the values of the thin films can be obtained, as indicated by the dotted line in figure 5(b). Although overestimating the conductivity, this model is qualitatively comparable to the experimental values. However, the discrepancy between model and the experiment suggests that the Fe layer may be less well defined than it seems from the EDS maps, and not continuous in the sample. An additional factor decreasing the conductivity is that during the measurement, the current needs to pass from the contact through the Fe_{1-x}O layer in thickness direction to reach the Fe-layer, thereby increasing resistivity. Nevertheless, considering the small thickness of the Fe-layer compared to the overall film thickness, these interfacial layers seem to be controlling for charge transport in the Fe_{1-x}O thin films.

Another approach to understand the difference of electrical conductivity between the thin films and single crystals are the grain boundaries, which exists in the thin films in contrast to the single crystalline reference samples. Reports in literature on Fe_3O_4 films have shown that the grain boundaries are better electrical conductors than the bulk grains [31, 32]. As the crystal structures of both Fe_{1-x}O and Fe_3O_4 are similar, one may deduce a similarly better conductivity in grain boundaries for Fe_{1-x}O films compared to bulk.

4. Conclusions

By optimizing the O_2/Ar flow ratio as well as the pressure–distance product, Fe_{1-x}O films with 96 vol.% phase purity have been achieved and the impurity phase being $\alpha\text{-Fe}$. Considering the low pressure–distance product, the formation of Fe_{1-x}O is understood to be surface controlled. While the resistivity of the sample with 96 vol.% Fe_{1-x}O exhibits a temperature dependence of electrical resistivity that is expected for wüstite, samples with larger impurity phase contents are better electronic conductors with an activation energy for charge transport which is half of the value for the 96 vol.% wüstite sample. The origin for this may be found in the microstructure, where Fe-rich layers at the substrate–film interface may serve as additional conduction paths and have been observed for samples with high impurity content. To understand the formation of these layers, the initial stages of nucleation during growth of Fe_{1-x}O thin films need to be investigated in future studies.

Data availability statement

The data cannot be made publicly available upon publication because they are not available in a format that is sufficiently accessible or reusable by other researchers. The data that support the findings of this study are available upon reasonable request from the authors.

Acknowledgments

The research leading to this result has been supported by the RADIATE project under the Grant Agreement 824096 from the EU Research and Innovation program HORIZON 2020. Financial support of the Tandem Accelerator Infrastructure at Uppsala University by VR-RFI (Contract #2019–00191) is gratefully acknowledged. GD is thankful for funding by the ERC Advanced Grant GB CORRELATE (Grant Agreement 787446). Dennis Klapproth is acknowledged for technical support with the PVD cluster at MPIE.

Author contributions

S E: Conceptualization, Investigation, Formal analysis, Writing—original draft; N N: Investigation, Formal analysis; N C: Investigation; D P: Investigation, Formal analysis; J P B: Conceptualization, Supervision; G D: Conceptualization, Supervision; all authors: Writing—Review & Editing

ORCID iDs

D Primetzhof  <https://orcid.org/0000-0002-5815-3742>

J P Best  <https://orcid.org/0000-0003-4728-2052>

References

- [1] Kim S-H et al 2021 Influence of microstructure and atomic-scale chemistry on the direct reduction of iron ore with hydrogen at 700 °C *Acta Mater.* **212** 116933
- [2] Ma Y et al 2022 Hierarchical nature of hydrogen-based direct reduction of iron oxides *Scr. Mater.* **213** 114571
- [3] Charvin P, Abanades S, Flamant G and Lemort F 2007 Two-step water splitting thermochemical cycle based on iron oxide redox pair for solar hydrogen production *Energy* **32** 1124–33
- [4] Pernicone N, Ferrero F, Rossetti I, Forni L, Canton P, Riello P, Fagherazzi G, Signoretti M and Pinna F 2003 Wüstite as a new precursor of industrial ammonia synthesis catalysts *Appl. Catal. A* **251** 121–9
- [5] Dimitrov D, Unruh K, Hadjipanayis G, Papaefthymiou V and Simopoulos A 2000 Defect clusters in Fe_{1-x}O and their ferrimagnetic properties *J. Appl. Phys.* **87** 7022–4
- [6] Gleitzer C 1997 Electrical properties of anhydrous iron oxides *Key Eng. Mater.* **125** 355–418
- [7] Molenda J, Stokłosa A and Znamirski W 1987 Transport properties of ferrous oxide Fe_{1-y}O at high temperature *Phys. Status Solidi b* **142** 517–29
- [8] Hillegas W J 1968 *Seebeck Coefficient and Electrical Conductivity Measurements on Doped and Undoped Wüstite* (Northwestern University) p 213
- [9] Neuschütz D and Towhidi N 1970 Die elektrische Leitfähigkeit von Wüstite *Arch. Eisenhüttenwes.* **41** 303–7
- [10] Toroker M C and Carter E A 2012 Hole transport in nonstoichiometric and doped wüstite *J. Phys. Chem. C* **116** 17403–13
- [11] Kerisit S and Rosso K M 2005 Charge transfer in FeO : a combined molecular-dynamics and ab initio study *J. Chem. Phys.* **123** 224712

- [12] Mauvernay B, Presmanes L, Capdeville S, de Resende V G, De Grave E, Bonningue C and Tailhades P 2007 Elaboration and characterization of Fe_{1-x}O thin films sputter deposited from magnetite target *Thin Solid Films* **515** 6532–6
- [13] Dimitrov D, Hadjipanayis G, Papaefthymiou V and Simopoulos A 1997 Magnetic properties and microstructure of Fe-O and Co-O thin films *IEEE Trans. Magn.* **33** 4363–6
- [14] Chin T S and Chiang N C 1997 Magnetic properties of sputtered Fe_{1-x}O and $\text{Fe}+\text{Fe}_3\text{O}_4$ thin films *J. Appl. Phys.* **81** 5250–2
- [15] Kim Y K and Oliveria M 1994 Magnetic properties of reactively sputtered Fe_{1-x}O and Fe_3O_4 thin films *J. Appl. Phys.* **75** 431–7
- [16] Muhammed Shameem P V, Mekala L and Kumar M S 2018 Structural and magnetic properties of non-stoichiometric Fe_{1-x}O thin films *AIP Conf. Proc.* **1942** 080077
- [17] BesTec GmbH 2022 P381–6'' HV/UHV multitechnique deposition cluster tool MPIE (available at: www.bestec-berlin.de/2014/deposition/4066/p381-hv-uhv-cluster-tool-mpie/)
- [18] de la Peña F et al 2021 HyperSpy v1.6.5 (available at: <https://zenodo.org/records/5608741>)
- [19] Ström P and Primetzhofer D 2022 Ion beam tools for nondestructive in-situ and in-operando composition analysis and modification of materials at the Tandem laboratory in Uppsala *J. Instrum.* **17** P04011
- [20] Zhang Y, Whitlow H J, Winzell T, Bubb I F, Sajavaara T, Arstila K and Keinonen J 1999 Detection efficiency of time-of-flight energy elastic recoil detection analysis systems *Nucl. Instrum. Methods Phys. Res. B* **149** 477–89
- [21] Janson M S 2004 CONTES instruction manual *Internal Report* Uppsala University
- [22] Miccoli I, Edler F, Pfnur H and Tegenkamp C 2015 The 100th anniversary of the four-point probe technique: the role of probe geometries in isotropic and anisotropic systems *J. Phys.: Condens. Matter* **27** 223201
- [23] Darken L S and Gurry R W 1945 The system iron-oxygen. I. The wüstite field and related equilibria *J. Am. Chem. Soc.* **67** 1398–412
- [24] Chambers S A 2000 Epitaxial growth and properties of thin film oxides *Surf. Sci. Rep.* **39** 105–80
- [25] Depla D and Leroy W P 2012 Magnetron sputter deposition as visualized by Monte Carlo modeling *Thin Solid Films* **520** 6337–54
- [26] Thornton J A 1988 Structure-Zone Models Of Thin Films *Proc. SPIE* **0821**
- [27] Messier R, Giri A P and Roy R A 1984 Revised structure zone model for thin film physical structure *J. Vac. Sci. Technol. A* **2** 500–3
- [28] Thornton J A 1986 The microstructure of sputter-deposited coatings *J. Vac. Sci. Technol. A* **4** 3059–65
- [29] Gartstein E and Mason T O 1982 Reanalysis of wüstite electrical properties *J. Am. Ceram. Soc.* **65** C-24–C-26
- [30] Bardeen J 1940 Electrical conductivity of metals *J. Appl. Phys.* **11** 88–111
- [31] Myers J, Nicodemus T, Zhuang Y, Watanabe T, Matsushita N and Yamaguchi M 2014 Characterization of grain boundary conductivity of spin-sprayed ferrites using scanning microwave microscope *J. Appl. Phys.* **115** 17A506
- [32] Xing Y, Myers J, Obi O, Sun N X and Zhuang Y 2012 Excessive grain boundary conductivity of spin-spray deposited ferrite/non-magnetic multilayer *J. Appl. Phys.* **111** 07A512